Supporting Information for "Upper Mantle deformation beneath the Northeastern part of Indian plate from Shear-wave splitting analysis"

Jyotima Kanaujia[1,2]*, G.Surve[1]

[1]Indian Institute of Geomagnetism, Navi Mumbai, India

[2]CSIR-National Geophysical Research Institute, Hyderabad 500007, India

Contents of this file

1. Tectonic setting of Northeast India
2. Previous results of seismic anisotropy in NE India
3. Seismic anisotropy – an effective tool to investigate mantle dynamics
4. Methodology for Shear wave splitting analysis
5. Methodology for Depth localization of anisotropy
6. List of figures. Figures S1 to S7.

Figure S1: Topographic map of North India showing the major tectonic units and major and regional thrust/fault systems (adopted from Mitra, Priestley, Bhattacharyya, and Gaur (2005); Angelier and Baruah (2009)). Orange bars represent measurements from more than 20 previous investigations (Wustefeld et al., 2009, http://splitting.gm.univmontp2.fr/DB/public/searchdatabase.html) Red triangles indicate stations from the newly installed IIG network, Blue circles represent stations with all Null measurements from previous studies. IYS: Indus Yalu Suture; BNS: Bangong Nujiang Suture; MBT: Main Boundary Thrust; EHS: Eastern Himalayan Syntaxis; OF: Oldham fault; DuF: Dudnoi fault; CMF: Churachandpur-Mao fault. The rectangle in the inset map outlines the study area shown in the main figure.

Figure S2: Examples of splitting observations. The station code and event information are indicated at the top panel of each figure. On the top left panel, the radial (R) and transverse (T) components of the SKS phase before correction is shown; the shaded part marks the selected SKS waveform window. Four diagrams in the lower panel show the fast and slow split shear wave (dashed and continuous lines, respectively) before and after correction for the best-calculated delay time, corresponding particle motions, and the contour plot of energy on the transverse component as a function of δt (s) and strike (°). The shaded contour represents a 95 % confidence level.

Figure S3: Examples of Null measurements. The station code and event information are indicated at the top panel of each figure. Other details are the same as in Figure S1. Note the negligible energy at T component (a), linear particle motions (d), and elongated ellipsoid for delay time values (e).

Figure S4: (a)Individual splitting results obtained at each station. The orientation of the bars represents the FDP and the length of the bars scales with associated delay times. Bars are color-coded according to the results from different XKS phases; Blue bars: SKS, Green bars: SKKS, and Cyan bars: PKS phases. Stations with no splitting results are marked as white circles, only null results were obtained on these stations. (b) Station-wise null results are plotted in this map.

Figure S5: (a) The map shows the apparent station-averaged FPDs(ϕ) plotted at station locations (blue bars are FPD results from IIG stations, orange bars from Saikia et al. (2018) stations). Bars are scaled with delay times and the oriented in the FPD (ϕ), plotted with associated errors as fans. The small black circles without bars are the stations with only null measurements. (b) The map shows the station-wise Null measurements plotted at station locations (Nulls from SKS, SKKS, and PKS are represented by blue, green, and cyan bars, respectively). (c) Histogram of the estimated FPD ϕ and delay times δt for the whole dataset. A maximum number of observations indicates the FPD direction lies between 40° and 80° and delay times between 0.7s and 1.25s. The rightmost corner histogram shows the Null results. Null results clearly show the bidirectional distribution of the observed null ϕ direction.

Figure S6: Map of linear interpolation of delay time plotted as a continuous surface plotted on the topographic map of the region with various fault/shear zones. The delay times from individual measurements are plotted above the 200km ray piercing points.

Figure S7: Azimuthal variations of the fast polarization (upper panel) and delay times (lower panel) for stations (a)Group1 (ϕ_U =60, δt$_U$ =0.5; ϕ_L =-66, δt$_L$ =1.2), (b)Group 2 (ϕ_U =60, δt$_U$ =0.7; ϕ_L =-66, δt$_L$ =0.9), (c)AZWL (ϕ_U =35, δt$_U$ =0.4; ϕ_L =15, δt$_L$ =0.7), (d)SHLS (ϕ_U =90, δt$_U$ =0.4; ϕ_L =16, δt$_L$ =1.2), and (e)SILS (ϕ_U =54, δt$_U$ =0.4; ϕ_L =-69, δt$_L$ =1.5). Variation of Fast polarization (FPD) and delay time against the backazimuth (BAZ) are plotted with modulo 90° BAZ values. The curve lines are the best fit model for the apparent splitting measurements as a function of BAZ in the presence of two layers of anisotropy. These best-fit parameters are listed in table 1.

7. List of Tables. S1 to S4.

Table S1: Individual splitting measurements at all stations.(Files uploaded separately)

Table S2: Individual null measurements at all stations.(Files uploaded separately)

Table S3: Single layer (apparent) splitting results at individual stations along with the observed Null directions. Stations written in bold letters are the stations from NE-network of IIG.

Table S4: Double layer anisotropy parameters.

1. Tectonic setting of Northeast India

The Himalayan collision zone is characterized by the E-W aligned Main Boundary Thrust (MBT) and the NE-SW trending Main Central Thrust (MCT), resulting from the maximum shear (extensional shear) in the respective directions. This extensional shear is produced by N–S compression of the underthrusting Indian plate beneath the Eurasian counterpart. At the eastern end, the Himalayan collision belt bends over the syntaxis in the NW–SE direction and interacts with the Indo-Burma subduction arc almost orthogonally (Figure S1). The Indo-Burma subduction boundary is oblique to the Indian plate motion direction (Satyabala, 2003). Away from these plate margins, the E–W oriented Shillong plateau and the Mikir Hills stand out as distinct topographic features south of the sediment-filled foredeep region that resulted from the shallow underthrusting along the Himalayan front (Figure S1, 1). This region is punctuated with several faults; prominent of them being the Oldham, Dauki, and Kopili, marking the northern, southern, and eastern boundaries of the Shillong plateau (Figure 1). The east-west oriented Shillong Plateau has an old cratonic root which is a part of the Archean Indian subcontinent (Vernant et al., 2014). Though the Uplift of the Himalaya and underthrusting of the Indian plate continues at a rate of 2 cm/year, active subduction at the Indo–Burmese arc and the formation mechanism of the Shillong plateau are debatable (Satyabala, 1998; Rao & Kumar, 1997; Bilham & England, 2001). The Shillong plateau uplift, which continues to date, started during the lower Cretaceous period, and its tectonic evolution is closely interlinked with the outpouring of the Sylhet Traps. Some authors advocate that active subduction below Indo-Burman ranges ceased, and presently the east dipping India plate is dragged northeastward (Ni et al., 1989; Sahu et al., 2006; Kundu & Gahalaut, 2013; Rao & Kumar, 1999; Rao & Kalpna, 2005). However, others argue for an active subduction in the Indo-Burmese convergence zone (Copley & McKenzie, 2007; Steckler et al., 2008, 2016; A. Kumar et al., 2015). The role of pre-existing lithospheric structures, mantle flow movement and dynamic lithospheric stresses in the geodynamic evolution of the region are debated. Orientation and strength of seismic anisotropy are often used to resolve the role of these mechanisms. The motion along the lithospheric scale faults can induce alignment of minerals resulting in detectable seismic anisotropy within the lithosphere.

2. Previous results of seismic anisotropy in NE India

Previous researchers have carried out various studies for the Indian subcontinent (Hirn et al., 1995; McNamara et al., 1994; Sandvol et al., 1997; Ramesh & Prakasam, 1995; Huang et al., 2000; Singh et al., 2006; Heintz et al., 2009; L. Liu et al., 2019). Sandvol et al. (1997) suggested a transversely isotropic Indian plate since no evidence of anisotropy was found in the eastern Himalaya and Tibet, except for the region 100 km north of the Indus–Tsangpo suture zone. However, Ramesh and Prakasam (1995); Ramesh et al. (1996) presented the first results, which characterized the Indian lithosphere with consistent NNE–SSW directional anisotropy. Chen and Ozalaybey (1998) inferred a purely isotropic Indian subcontinent based on limited measurements from stations HYB (Hyderabad) and SHIO (located on the Shillong plateau, Northeast India). Heintz et al. (2009); M. R. Kumar and Singh (2008) carried out anisotropy measurements on a continental scale and obtained consistent results closer to the collision front in northern India. They explained the newly found anisotropy in terms of foliation planes of the Himalayan fold and thrust belts. Most seismic anisotropic studies in the Indian region are concentrated on the Indian subcontinent and the Himalaya. Only a few studies have explored the anisotropic signatures in Northeast India at a regional scale (e.g., (Hazarika et al., 2013)-Eastern Himalaya syntaxis (EHS); (Roy et al., 2014); (Saikia et al., 2010)-Arunanchal Pradesh and adjoining regions; (L. Liu et al., 2019)-vicinity of EHS; (Mohanty & Mondal, 2020)-Shillong Plateau and Himalaya foothills). Two studies (Singh et al., 2006) and (Saikia et al., 2018) present anisotropy results for the whole of NE India. The very first detectable mantle anisotropy in the NE India region was reported by Singh et al. (2006). They found E–W directed anisotropy in the northeast Himalayan collision zone, N-S in the Indo-Burma convergence zone, and NE-SW in the Assam valley and Shillong plateau intraplate zone. (Saikia et al., 2018) reported similar results in the Assam valley and Shillong Plateau but weak orogen parallel anisotropy in the eastern Himalaya and Burmese arc regions. Recently, (L. Liu et al., 2019) proposed a geodynamic model based on the seismic anisotropy results in Eastern Himalayan Syntaxis and its adjoining regions. Their model supports active subduction at the Indo–Burman plate boundary and advocates the toroidal mantle flow induced by slab subduction and rollback beneath the Eastern Himalayan Syntaxis (EHS). Most of the stations used in (L. Liu et al., 2019) are located east and north of NE India. Despite all this available independent knowledge about the kinematics and the geodynamic implication of different tectonic units of NE India, a comprehensive study is required to decipher the mantle dynamics of the entire region as a whole and the interaction between different tectonic units.

3. Seismic anisotropy – an effective tool to investigate mantle dynamics

Over the past three decades, seismic anisotropy has emerged as a valuable tool for investigating the structure and dynamic processes in the Earth's interior. It provides information about the present and past deformation processes in the crust, the upper mantle, and lower mantle (Babuška & Cara, 1991; M. K. Savage, 1999; Fouch & Rondenay, 2006; Long & Silver, 2008). It also helps explore the rock textures within Earth's mantle and crust, capture present-day upper-mantle convection, and study the formation of lithospheric plates and the accretion of continents. Shear wave splitting (SWS) phenomena accurately represents seismic anisotropy. When a seismic shear wave travels through an anisotropic medium, it splits into two orthogonally polarised shear waves, one travelling faster than the other. The azimuthal polarisation of fast shear wave (fast polarization direction (FPD) ϕ) and the time difference (delay time δt) between these two waves are the two splitting parameters estimated by SWS analysis. The SWS analysis assumes a single horizontal layer of anisotropy at the receiver side. However, any observed variation of apparent ϕ and δt with the initial polarization of incident wave (backazimuth (BAZ) for XKS) points towards multiple layers of anisotropy or tilted layer of anisotropy (K. Savage & Silver, 1993; M. K. Savage, 1999). SWS measurements offer an excellent lateral resolution of fewer than 50 km, albeit a poor vertical resolution (Savage 1999). Shear wave splitting is usually investigated using core-refracted phases XKS (SKS, SKKS, PKS, and PKKS). The SWS measurements from XKS phases are generally interpreted in terms of the upper mantle and lithospheric anisotropy. The relation between seismic anisotropy and the deformation mechanism is that when an anisotropic media is deformed in the active shear stress conditions, then the anisotropic minerals like olivine tend to align in the direction of maximum shear. The FPD of seismic waves is ascribed to this Lattice preferred orientation (LPO) of anisotropic minerals in the upper mantle (Silver, 1996; M. K. Savage, 1999), and the shape-preferred orientation (SPO) of fluid-filled cracks or compositional layering in the crust (Crampin, 1987). The FPDs align with the direction of maximum shear, which is along the mantle flow direction in the asthenospheric mantle, perhaps providing a proxy for plate motion direction. Anisotropic minerals in the lithosphere are likely to have a texture imprinted into them during past tectonic deformation events. Silver (1996) inferred that the anisotropy directions in the lithosphere result from post-tectonic thermal relaxation, which is frozen in the lithosphere. The continental seismic anisotropy is interpreted in terms of past tectonic events, active plate motion direction, or a combination of both mechanisms. Possible differentiation between these two mechanisms provides clues about the present plate motion direction and past deformation processes (Conrad et al., 1987). These observations provide a better understanding of the long-term behavior of a rheologically complex lithosphere, including changes in plate motions and the formation of the continents. Transitions between geologically recent deformation and frozen-in anisotropy from older tectonic motions are reflected in layering (Plomerová & Babuška, 2002; Yuan & Romanowicz, 2010).

4. Methodology: Shear wave splitting analysis

To enhance the signal-to-noise ratio (SNR), the waveforms were filtered using a bandpass Butterworth filter between 0.02 Hz and 0.25 Hz. The data at each station are chosen based on specific criteria viz. 1) a high signal-to-noise ratio ($\geq$4.0) 2) small amplitude of the XKS phase on the vertical component and 3) large time gap ($\geq$15 s) with the next significant phase arrival, implying a distinct SKS or SKKS phase. A narrow time window within ±15-20 s on either side of the theoretical SKS/SKKS/PKS phase arrival time (IASP91 model (B. Kennett & Engdahl, 1991; B. L. N. Kennett et al., 1995)) is selected to ensure proper phase identification. A total of 927 waveforms from 301 teleseismic earthquakes were selected using these criteria, containing 82 PKS phases, 152 SKKS phases, and 693 SKS phases.

The SplitLab MATLAB toolbox (Wüstefeld et al., 2008) is used to estimate the shear wave splitting parameters (ϕ, δt), simultaneously using the rotation correlation (Bowman & Ando, 1987) and the energy minimization (Silver & Chan, 1991) methods. The former is based on the fact that the radial and transverse components of the shear wave have orthogonal polarizations and different velocities, but have the same shape. Hence, to determine the splitting parameters, the value of cross-correlation coefficient is used to maximize the similarity of the slow and fast waves as a function of the delay time between them, using a grid search. The grid search is carried out over a range of ϕ from -90° to 90° and δt between 0 and 4s. The latter method also uses a grid search over the same parameter range and selects the pair (ϕ, δt) that minimizes the energy on the transverse component when corrected for splitting. Figure S2 presents three examples of the original and corrected data. The grid search yields a contour plot of the energy on the corrected transverse component for each FPD-delay time pair, allowing the uncertainties of each splitting parameter to be quantified. A well-constrained split result is recognized by a well-defined elliptical particle motion (Figure S2 (d)) before correction and a well-defined minima contour on the energy plot (Figure S2 (e)). In some cases, the minima contour on the energy plot is highly elongated along the delay time axis (Figure S3 (e)). These measurements have nearly no signal on the transverse component accompanied by a near linear particle motion before correction for splitting and are classified as Null (Wuestefeld & Bokelmann, 2007). Figure S3 shows three examples of these measurements. The splitting and Null measurements are classified into different quality classes according to the following criteria.

Measurements with errors more than 0.5 s in delay times and 20° in FPDs are discarded from further interpretation. A good agreement between the splitting parameters using the two methods is observed for the remaining data, with typical differences being less than 20° for FPD and 0.3 s for delay times. Each splitting result was then rated as Good, Fair, or Poor considering the quality of the data used, signal-to-noise ratio (SNR), clarity of the SKS waveform, apparent elliptical particle motion, quality of energy minimization contour plot/cross-correlation plot and the agreement between the results obtained from the two methods. For results classified as (i) good : Quality factor $\geq$0.90 and the difference between FPDs and delay times obtained using both the methods is $\leq$20° and $\leq$0.3 s, respectively; (ii) fair : 0.75$\leq$Quality factor$\leq$0.90, and FPDs and delay times differences are $\leq$30° and $\leq$0.5 s respectively. Others are marked as poor splitting results. Similarly, Null measurements are ranked as good or fair based on the SNR being $\geq$5 and the uncorrected particle motion being linear. Since the results from both the methods are in good agreement, results obtained from Silver and Chan (1991) method are only reported in this study.

4.1. Depth localization of anisotropy

The anisotropic layer depth can be constrained using various methodologies, spatial coherency analysis (K. H. Liu & Gao, 2011), finite frequency analysis (Mondal & Long, 2019), employing surface-wave data or multiple core-reflected phases SKS and SKKS. (K. H. Liu & Gao, 2011) presented a simplified procedure by measuring the spatial coherency of the splitting parameters. This spatial coherency analysis is used here to evaluate the depth of the anisotropic layer. A detailed description is given in (Gao & Liu, 2012) and is briefly summarized here. Densely spaced stations in the study zone provide the necessary conditions to apply the spatial coherency technique to estimate the depth of anisotropy. The method assumes that the detected SWS is from a single horizontal layer of anisotropy with hexagonal symmetry and a horizontal symmetry axis. The approach is based on the intersecting fresnel-zone principle. The procedure starts with computing the geographic distribution of ray-piercing points at various depth sections from the surface to the 400 km depth in an increment of 5 km. At each depth level, the area covered by the ray-piercing points was then divided into rectangular blocks of area $D_x{}^{\circ} \times D_x{}^{\circ}$. The spatial variation factor, which is the dimensionless weighted sum of the circular standard deviation of the FPDs and the arithmetic standard deviation of the splitting times in rectangular blocks, is calculated for each depth section. The expression used for variation factor defined by (K. H. Liu & Gao, 2011)is given as:

$$F_v = \omega_\phi F_\phi + \omega_{\delta t} F_{\delta t} \tag{1}$$

where ω_ϕ and $\omega_{\delta t}$ are the weighting factors for FPD and delay time, respectively.

$$F_{\delta t} = \frac{1}{N} \sum_{i=1}^{N} \sqrt{\frac{1}{M_i - 1} \sum_{j=1}^{M_i} (\delta t_{i,j} - \overline{\delta t_i})} \tag{2}$$

and

$$F_\phi = \frac{1}{N} \sum_{i=1}^{N} \sqrt{-\frac{1}{2} \sum_{j=1}^{M_i} log(R_i)} \tag{3}$$

where

$$R_i = [\frac{1}{M_i} \sum_{j=1}^{M_i} cos(2\phi_{i,j})]^2 + [\frac{1}{M_i} \sum_{j=1}^{M_i} sin(2\phi_{i,j})]^2 \tag{4}$$

N is the number of blocks, M_i is the number of measurements for the i-th block, $\phi_{i,j}$ and $\delta t_{i,j}$ are the j-th FPD and delay time in the i-th block. $\overline{\delta t_i}$ is the average delay time over all the measurements in the i-th block.

References

Angelier, J., & Baruah, S. (2009, 07). Seismotectonics in northeast india: A stress analysis of focal mechanism solutions of earthquakes and its kinematic implications. *Geophys. J. Int*, *178*, 303–326.

Babuska, V., & Cara, M. (1991). *Seismic anisotropy in the earth* (Vol. 10). Kluwer Academic Publishers, Dordrecht, The Netherlands.

Bilham, R., & England, P. (2001). Plateau 'pop-up' in the great 1897 assam earthquake. *Nature*, *410*(6830), 806-809.

Bowman, J. R., & Ando, M. (1987). Shear-wave splitting in the upper-mantle wedge above the tonga subduction zone. *Geophysical Journal International*, *88*(1), 25–41.

Chen, W. P., & Ozalaybey, S. (1998). Correlation between seismic anisotropy and bouguer gravity anomalies in tibet and its implications for lithospheric structures. *Geophysical Journal International*, *135*(1), 93–101.

Conrad, C. P., Behn, M. D., & Silver, P. G. (1987). Geological and industrial implications of extensive-dilatancy anisotropy. *Nature*, *328*(6), 491–496.

Copley, A., & McKenzie, D. (2007, 05). Models of crustal flow in the india-asia collision zone. *Geophysical Journal International*, *169*, 683–698.

Crampin, S. (1987). Geological and industrial implications of extensive-dilatancy anisotropy. *Nature*, *328*(6), 491–496.

Fouch, M., & Rondenay, S. (2006). Seismic anisotropy beneath stable continental interiors. *Phys. Earth Planet. Inter.*, *158*, 292–320.

Gao, S. S., & Liu, K. H. (2012). Anisdep: A fortran program for the estimation of the depth of anisotropy using spatial coherency of shear-wave splitting parameters. *Computers and Geosciences*, *49*, 330–333.

Hazarika, D., Yadav, D. K., Sriram, V., & Rai, A. (2013). Upper mantle anisotropy beneath northeast india-asia collision zone from shear-wave splitting analysis. *International Journal of Earth Sciences*, *102*(7), 2061–2076.

Heintz, M., Kumar, V. P., Gaur, V. K., Priestley, K., Rai, S. S., & Prakasam, K. S. (2009). Anisotropy of the indian continental lithospheric mantle. *Geophysical Journal International*, *179*(3), 1341–1360.

Hirn, A., Jiang, M., & Sapin, M. e. a. (1995). Seismic anisotropy as an indicator of mantle flow beneath the himalayas and tibet. *Nature*, *375*, 571–574.

Huang, W. C., Ni, J. F., Tilmann, F., Nelson, D., Guo, J., & Zhao, W. e. a. (2000). Seismic polarization anisotropy beneath the central tibetan plateau. *Journal of Geophysical Research*, *105*(B12), 27,979-27,989.

Kennett, B., & Engdahl, E. (1991). Travel times for global earthquake location and phase identification. *Geophys J Int*, *105*, 429-465.

Kennett, B. L. N., Engdahl, E. R., & Buland, R. (1995). Constraints on seismic velocities in the earth from travel times. *Geophys J Int*, *122*, 108–124.

Kumar, A., Mitra, S., & Suresh, G. (2015). Seismotectonics of the eastern himalayan and indo-burman plate boundary systems. *Tectonics*, *34*(11), 2279-2295.

Kumar, M. R., & Singh, A. (2008). Evidence for plate motion related strain in the indian shield from shear wave splitting measurements. *Journal of Geophysical Research: Solid Earth*, *113*(B08306). doi: doi:10.1029/2007JB005128

Kundu, B., & Gahalaut, V. K. (2013). Tectonic geodesy revealing geodynamic complexity of the indo-burmese arc region, north east india. *CURRENT SCIENCE*, *104*(7), 920-933-1693.

Liu, K. H., & Gao, S. S. (2011). Estimation of the depth of anisotropy using spatial coherency of shear-wave splitting parameters. *Bulletin of the Seismological Society of America*, *101*, 2153–2161.

Liu, L., Gao, S. S., Liu, K. H., Li, S., Tong, S., & Kong, F. (2019). Toroidal mantle flow induced by slab subduction and rollback beneath the eastern himalayan syntaxis and adjacent areas. *Geophysical Research Letters*, *46*, 11080-11090.

Long, M. D., & Silver, P. G. (2008). The subduction zone flow field from seismic anisotropy: A global view. *Science*, *319*(5861), 315–318.

McNamara, D. E., Owens, T. J., & Silver, P. G. e. a. (1994). Shear wave anisotropy beneath the tibetan plateau. *J Geophys Res*, *99*, 13655–13665.

Mitra, S., Priestley, K., Bhattacharyya, A., & Gaur, V. (2005). Crustal structure and earthquake focal depths beneath northeastern india and southern tibet. *Geophys. J. Int.*, *160*(1), 227-248.

Mohanty, D., & Mondal, P. (2020). Disparate behaviour of deformation patterns beneath northeast indian lithosphere inferred from shear wave splitting analysis,. *Physics of the Earth and Planetary Interiors*, *298*, 106315.

Mondal, P., & Long, M. D. (2019). A model space search approach to finite-frequency sks spliting intensity tomography in a reduced parameter space. *Geophys. J. Int.*, *217*, 238–256.

Ni, J., Speziale, M., Bevis, M., Holt, W., Wallace, T., & Seager, W. (1989). Accretionary tectonics of burma and the three-dimensional geometry of the burma subduction zone. *Geology*, *17*, 68–71.

Plomerová, D. K., J., & Babuška, V. (2002). Mapping the lithosphere-asthenosphere boundary through changes in surface-wave anisotropy. *Tectonophysics*, *58*, 175-185.

Ramesh, D. S., Bharthur, R. N., Prakasam, K. S., Srinagesh, D., Rai, S. S., & Gaur, V. K. (1996). Predominance of plate motion-related strain in the south indian shield. *Curr. Sci.*, *70*(9), 843-847.

Ramesh, D. S., & Prakasam, K. S. (1995). Shear wave splitting observations from the indian shield. *In: Proc. Indian Acad. Sci. (Earth Planet. Sci.)*, *104*, 85-114.

Rao, N. P., & Kalpna. (2005). Deformation of the subducted indian lithospheric slab in the burmese arc. *Geophysical Research Letters*, *32*(5).

Rao, N. P., & Kumar, M. R. (1997). Uplift and tectonics of the shillong plateau, northeast india. *J. Phys. Earth*, *45*, 167-176.

Rao, N. P., & Kumar, M. R. (1999). Evidences for cessation of indian plate subduction in the burmese arc region. *Geophysical Research Letters*, *26*(20), 3149-3152.

Roy, S., Kumar, M., & Srinagesh, D. (2014). Upper and lower mantle anisotropy inferred from comprehensive sks and skks splitting measurements from india. *Earth Planet. Sci. Lett.*, *392*, 192-206.

Sahu, V. K., Gahalaut, V. K., Rajput, S., Chadha, R. K., Laishram, S. S., & Kumar, A. (2006). Indo-burmese arc region: implications from the myanmar and southeast asia gps measurements. *CURRENT SCIENCE*, *90*(12), 1688-1693.

Saikia, D., Kumar, M. R., Singh, A., K., R. S., S., R. P., & Lyngdoh, A. C. (2018). Mantle deformation in the eastern himalaya, burmese arc and adjoining regions. *Geochemistry, Geophysics, Geosystems*, *19*, 4420-4432.

Saikia, D., Kumar, M. R., Singh, A., Mohan, G., & Dattatrayam, R. S. (2010). Seismic anisotropy beneath the indian continent fromsplitting of direct s waves. *Journal of Geophysical Research*, *115*, B12315.

Sandvol, E., Ni, J., Kind, R., & Zhao, W. (1997). Seismic anisotropy beneath the southern himalayas-tibet collision zone. *Journal of Geophysical Research*, *102*((B8)), 17,813-17,823.

Satyabala, S. P. (1998). Subduction in the indo-burma region: Is it still active? *Geophys. Res. Lett.*, *25*, 3189– 3192.

Satyabala, S. P. (2003). Oblique plate convergence in the indo-burma (myanmar) subduction region. *Pure appl. geophys*, *160*, 1611–1650.

Savage, K., & Silver, P. (1993). Mantle deformation and tectonics: constraints from seismic anisotropy in the western united states. *Phys. Earth planet. Inter.*, *78*(3), 207–227.

Savage, M. K. (1999). Seismic anisotropy and mantle deformation: What have we learned from shear wave splitting? *Reviews of Geophysics*, *37*(1), 65-106.

Silver, P. G. (1996). Seismic anisotropy beneath the continents: Probing the depths of geology. *Annual Review of Earth and Planetary Sciences*, *24*, 385–432. Retrieved from `https://doi.org/10.1029/91JB00899`

Silver, P. G., & Chan, W. W. (1991). Shear wave splitting and subcontinental mantle deformation. *Journal of Geophysical Research: Solid Earth*, *96*, 16,429-16,454.

Singh, A., Kumar, M. R., Raju, P. S., & Ramesh, D. S. (2006). Shear wave anisotropy of the northeast indian lithosphere. *Geophysical Research Letters*, *33*, L16302.

Steckler, M., Akhter, S., & Seeber, L. (2008, 09). Collision of the ganges-brahmaputra delta with the burma arc: Implications for earthquake hazard. *Earth and Planetary Science Letters*, *273*, 367-378.

Steckler, M., Mondal, D., Akhter, S., Seeber, L., Feng, L., Gale, J., ... Howe, M. (2016, 07). Locked and loading megathrust linked to active subduction beneath the indo-burman ranges. *Nature Geoscience*, *9*, 11-2016.

Vernant, P., Bilham, R., Szeliga, W., Drupka, D., Kalita, S., Bhattacharyya, A. K., ... Berthet, T. (2014). Clockwise rotation of the brahmaputra valley relative to india: Tectonic convergence in the eastern himalaya, naga hills and shillong plateau. *Journal of Geophysical Research: Solid Earth*, *119*(8), 6558-6571.

Wuestefeld, A., & Bokelmann, G. (2007, 08). Null detection in shear-wave splitting measurements. *Bulletin of The Seismological Society of America*, *97*, 1204-1211.

Wustefeld, A., Bokelmann, G. H. R., Barruol, G., & Montagner, J. P. (2009). Identifying global seismic anisotropy patterns by correlating shear-wave splitting and urface waves data. *Phys. Earth Planet. Int*, *176*(3-4), 198-212.

Wüstefeld, A., Bokelmann, G., Zaroli, C., & Barruol, G. (2008). Splitlab: A shear-wave splitting environment in matlab. *Computers and Geosciences*, *34*(5), 515–528.

Yuan, H., & Romanowicz, B. (2010). Lithospheric layering in the northamerican continent. *Nature*, *466*, 1063–1069.

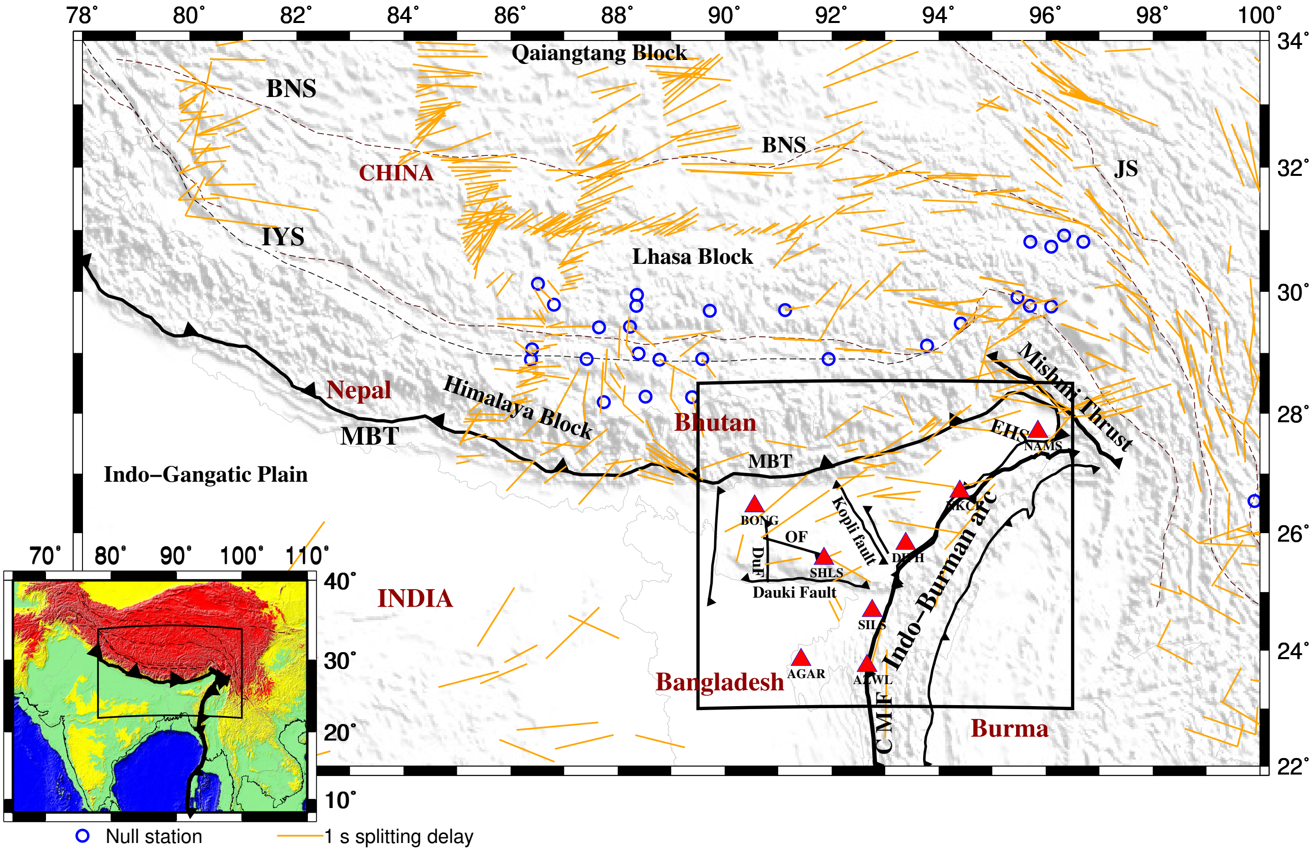

Figure S1. Topographic map of North India showing the major tectonic units and major and regional thrust/fault systems (adopted from Mitra et al. (2005); Angelier and Baruah (2009)). Orange bars represent measurements from more than 20 previous investigations (Wustefeld et al. (2009); http://splitting.gm.univmontp2.fr/DB/public/searchdatabase.html). Red triangles indicate stations from the newly installed IIG network, Blue circles represent stations with all Null measurements from previous studies. IYS: Indus Yalu Suture; BNS: Bangong Nujiang Suture; MBT: Main Boundary Thrust; EHS: Eastern Himalayan Syntaxis; OF: Oldham fault; DuF: Dudnoi fault; CMF: Churachandpur-Mao fault. The rectangle in the inset map outlines the study area shown in the main figure.

Table S3. Single layer (apparent) splitting results at individual stations along with the observed Null directions. Stations written in bold letters are the stations from NE-network of IIG

Tectonic divisions	**Station number**	**Station**	**Lat(°)**	**Long (°)**	**FPDs Φ(°)**	**δt (s)**	**Qf**	**# measurements**
Eastern Himalaya and EHS	1	TAWA	27.6028	91.857	49±10	0.82±0.4	0.9381	5
	2	BAIS	27.4638	92.1099	-86±16	1.05±0.5	0.8428	11
	3	DIRA	27.3578	92.2373	64±17	0.54±0.2	0.8187	5
	4	RUPA	27.2040	92.4012	69±19	0.82±0.4	0.7809	18
	5	ELEP	27.0931	92.5892	69±16	0.81±0.5	0.8454	13
	6	BICH	27.3047	92.6166	–	–	–	–
	7	PLZI	27.2931	92.7804	69±13	0.66±0.4	0.8965	5
	8	NAKP	27.646	93.0776	–	–	–	–
	9	SRLI	27.9523	93.1627	-41±00	0.48±0.0	1	1
	10	KOLO	27.9045	93.3529	83±37	0.94±0.1	0.1523	2
	11	SGRM	27.81	93.5324	-55±00	0.70±0.0	1	1
	12	PLIN	27.6888	93.6298	58±10	0.40±0.1	0.939	3
	13	DEED	27.5895	93.6761	69±13	0.68±0.2	0.8931	10
	14	ZIRO	27.5315	93.7788	69±12	0.79±0.2	0.906	5
	15	POTN	27.3366	93.8225	50±08	1.09±0.3	0.9584	4
	16	ITAN	27.144	93.7220	41±00	0.55±0.0	1	1
	17	NAVA	28.3615	93.6631	–	–	–	–
	18	KODA	28.2414	94.115	71±17	0.84±0.4	0.8228	2

	19	MENG	28.0999	94.1462	–	–	–	–
	20	TABA	27.9599	94.332	60±11	0.60±0.1	0.925	4
	21	PUCH	27.8434	94.1674	33±00	0.88±0.0	1	1
	22	BARI	27.946	94.4462	76±29	1.08±0.8	0.4923	3
	23	KAYI	28.4018	94.6882	-41±00	0.84±0.0	1	1
	24	TATO	28.5256	94.369	–	–	–	–
	25	BENE	28.1979	94.7242	–	–	–	–
	26	BAGR	28.007	94.7608	–	–	–	–
	27	RILU	27.8505	94.7933	55±04	0.82±0.3	0.9883	2
	28	PANG	28.2160	94.9999	–	–	–	–
	29	DITE	28.3624	95.0706	–	–	–	–
	30	RAMS	28.6584	95.002	-73±31	0.50±0.5	0.4037	2
	31	JENG	28.545	95.0610	-89±21	0.60±0.2	0.7307	3
	32	KAPU	29.0406	94.8747	73±20	0.90±0.3	0.7661	13
	33	MIGN	28.8502	94.7834	80±13	0.80±0.3	0.8957	10
Assam foredeep	34	**BONG**	26.4517	90.5575	75±14	0.42±0.2	0.8882	4
	35	DIBR	27.468	94.911	49±00	1.70±0.0	1	1
	36	JORH	26.743	94.2510	54±13	1.15±0.6	0.9027	2
	37	TEZP	26.617	92.8	70±18	0.91±0.3	0.795	13
	38	GUWA	26.193	91.6910	55±20	0.72±0.3	0.7446	9
	39	DHUB	26.02	89.995	77±04	0.78±0.3	0.9904	2
	40	TURA	25.517	90.224	14±00	0.55±0.0	1	1
Shillong Plateau	41	**SHLS**	25.566	91.855	-82±34	1.00±0.5	0.3046	6
	42	SHL	25.566	91.855	77±10	0.75±0.3	0.9368	4
	43	JAFL	25.179	92.0190	71±00	0.62±0.0	1	1

Bengal Basin	44	**AGAR**	23.8411	91.4247	-17±02	1.71±0.1	0.9971	2
	45	MPUR	24.604	90.03	–	–	–	–
	46	SKPR	24.319	90.171	–	–	–	–
	47	MANK	23.815	90.058	–	–	–	–
	48	BELO	23.248	91.447	–	–	–	–
	49	AGT	23.889	91.246	–	–	–	–
	50	SUST	24.923	91.834	–	–	–	–
	51	BARL	24.691	92.186	-54±07	0.61±0.0	0.9695	2
	52	JURI	24.5000	92.1400	-25±8	0.6±0.29	0.963	4
Indo-Burman Arc	53	**AZWL**	23.7372	92.6589	02±25	1.01±0.5	0.6241	11
	54	**DIPH**	25.8197	93.3822	31±00	0.80±0.0	1	1
	55	**NAMS**	27.6997	95.8503	61±27	1.06±0.5	0.5624	12
	56	**NKCR**	26.6989	94.3911	25±00	0.80±0.0	1	1
	57	**SILS**	24.6803	92.7547	65±14	0.74±0.5	0.8788	8
	58	AZL	23.738	92.69	–	–	–	–
	59	LKP	27.333	95.846	37±09	1.53±0.3	0.9458	40
	60	MOKO	26.321	94.516	33±22	1.19±0.2	0.7118	12
	61	SAIH	22.5000	93.0000	-04±13	1.40±0.3	0.8957	9
	62	KOHI	25.72	94.108	-41±24	0.93±0.3	0.6521	6
	63	IMP	24.831	93.946	-23±23	0.85±0.7	0.6639	3
	64	SILR	24.781	92.803	–	–	–	–

Table S4. Double layer anisotropy parameters. Stations grouped in Group 1 and 2 are shown in figure S7 as red dots

Station	**Upper layer (Weak)**		**Lower layer (Strong)**		**R^2**
	$\Phi_U(^\circ)$	$\delta\mathbf{t}_U$ **(s)**	$\Phi_L(^\circ)$	$\delta\mathbf{t}_L$ **(s)**	
AZWL	35±5	0.4±0.4	15±3	0.7±0.1	0.2738
SHLS	90±1	0.4±0.1	16±1	1.2±0.1	0.55104
SILS	54±5	0.4±0.1	-69±5	1.5±0.1	0.59597
Group–1 (KAPU, MIGN, RAMS, JENG)	60±4	0.5±0.05	-76±17	1.2±0.18	0.72025
Group–2 (BAIS, DIRA, RUPA, BICH, ELEP)	60±20	0.7±0.11	-76±13	0.9±0.25	0.85419

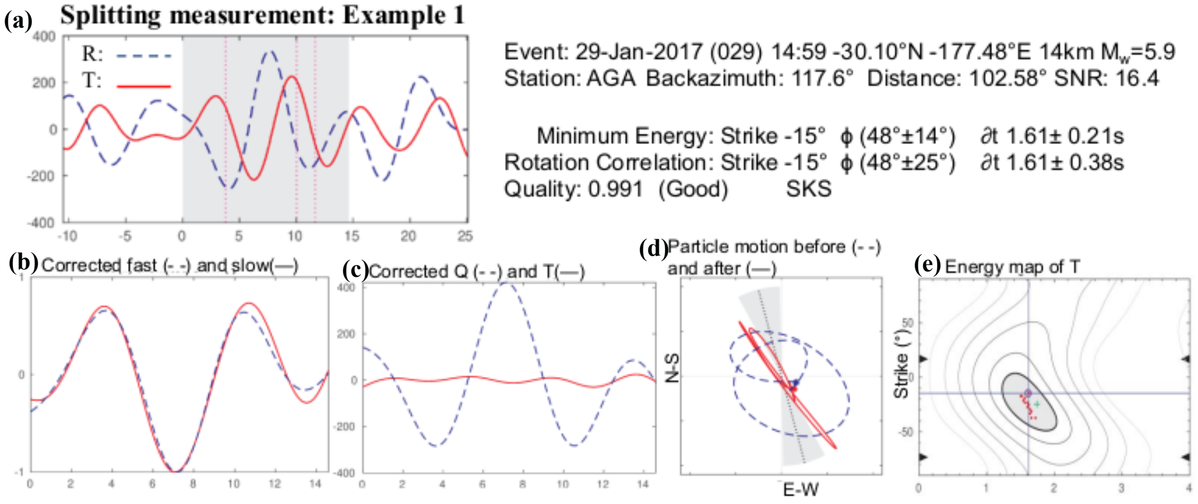

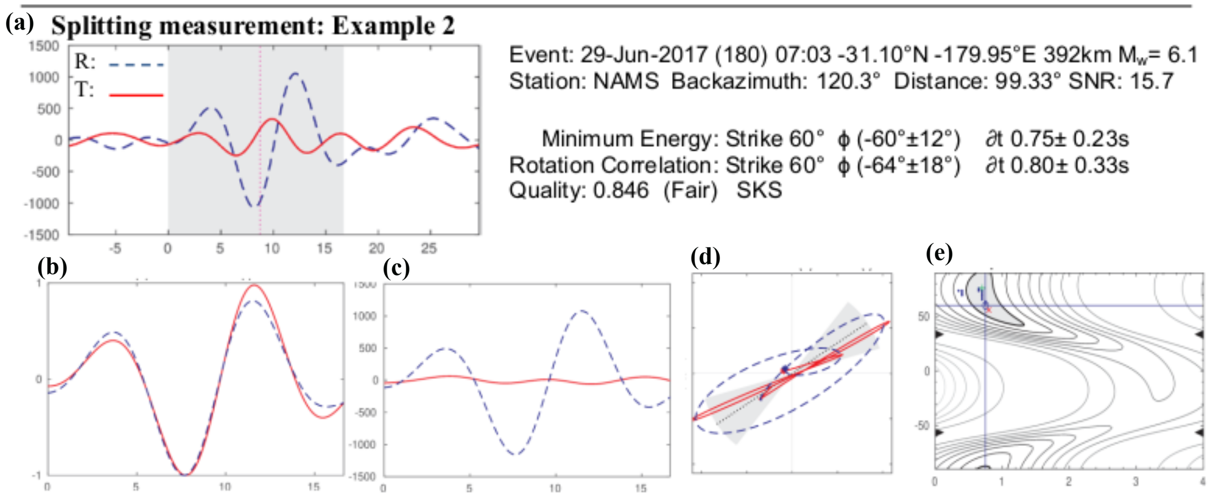

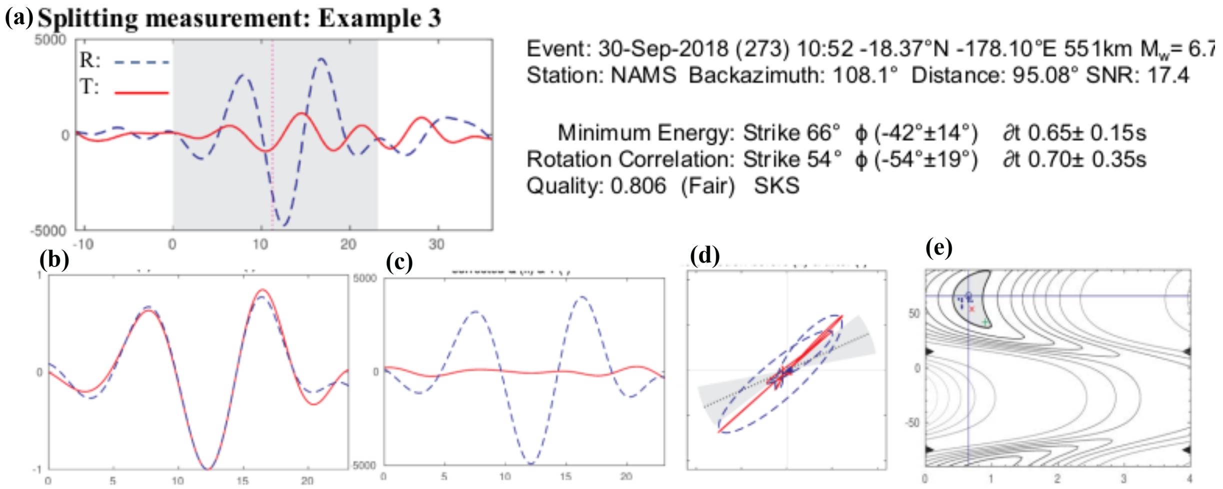

Figure S2. Examples of splitting observations. The station code and event information are indicated at the top panel of each figure. On the top left panel, the radial (R) and transverse (T) components of the SKS phase before correction is shown; the shaded part marks the selected SKS waveform window. Four diagrams in the lower panel show the fast and slow split shear wave (dashed and continuous lines, respectively) before and after correction for the best-calculated delay time, corresponding particle motions, and the contour plot of energy on the transverse

(a) **Null measurement: Example 1**

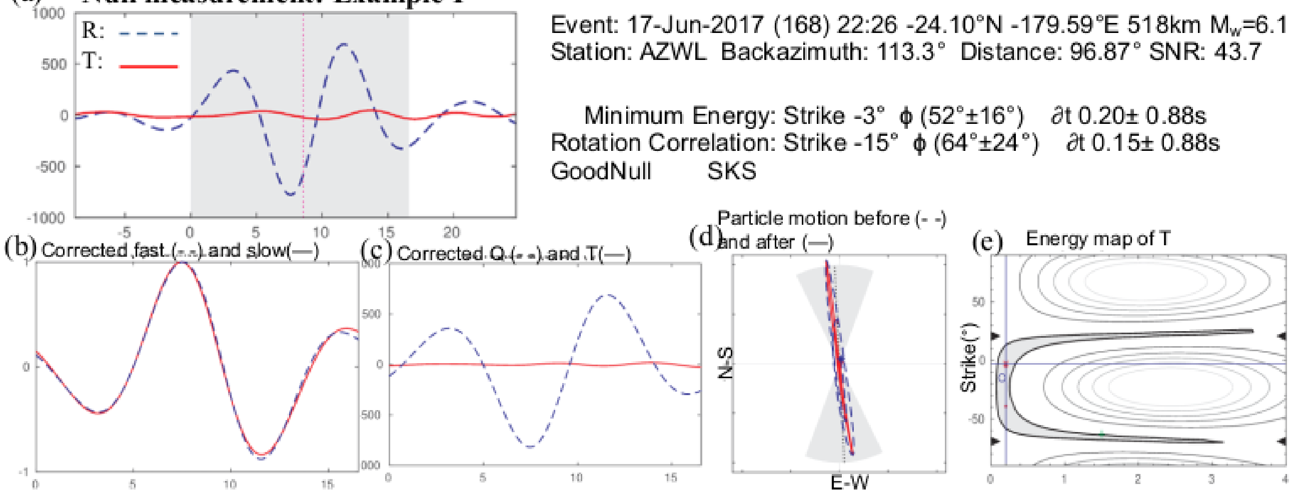

(a) **Null measurement: Example 2**

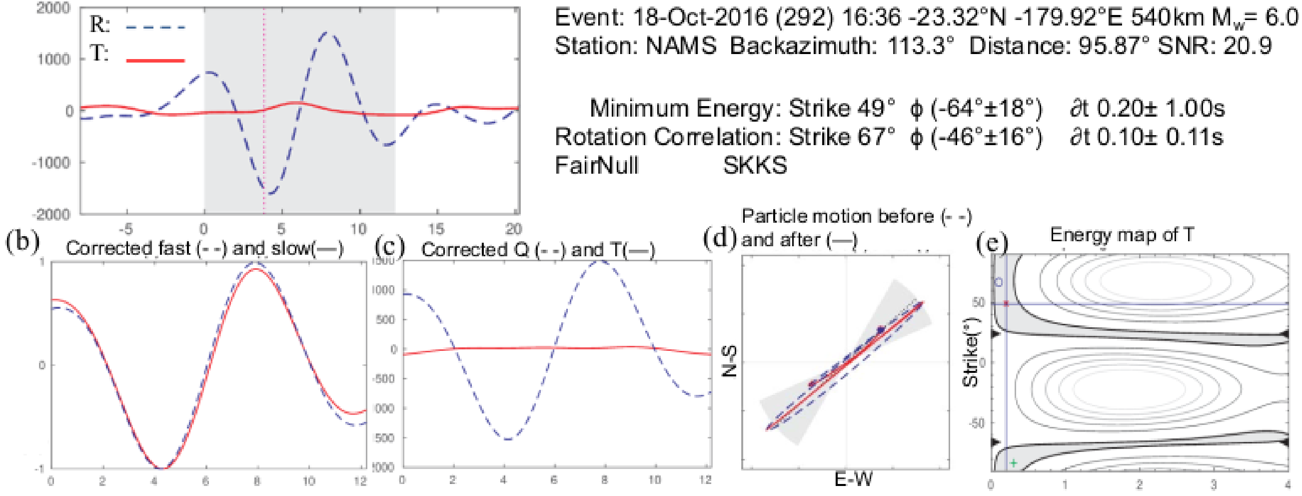

(a) **Null measurement: Example 3**

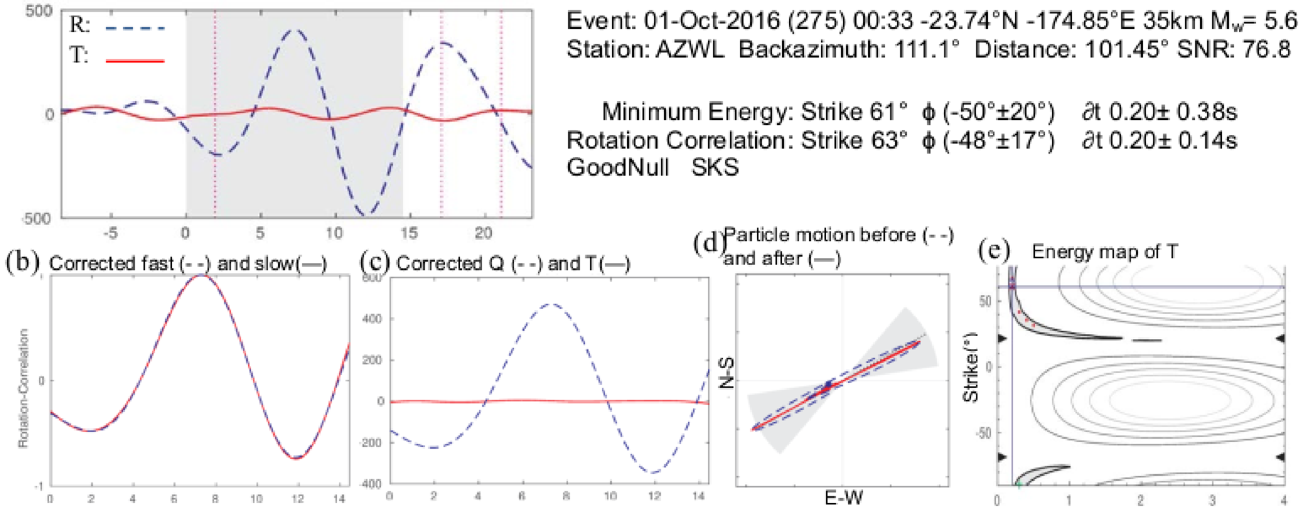

Figure S3. Examples of Null measurements. The station code and event information are indicated at the top panel of each figure. Other details are the same as in figure S1. Note the negligible energy at T component (a), linear particle motions (d), and elongated ellipsoid for delay time values (e).

Processed splitting individual results **Nulls**

Figure S4. (a)Individual splitting results obtained at each station. The orientation of the bars represents the FDP and the length of the bars scales with associated delay times. Bars are color-coded according to the results from different XKS phases; Blue bars: SKS, Green bars: SKKS, and Cyan bars: PKS phases. Stations with no splitting results are marked as white circles, only null results were obtained on these stations. (b) Station-wise null results are plotted in this map.

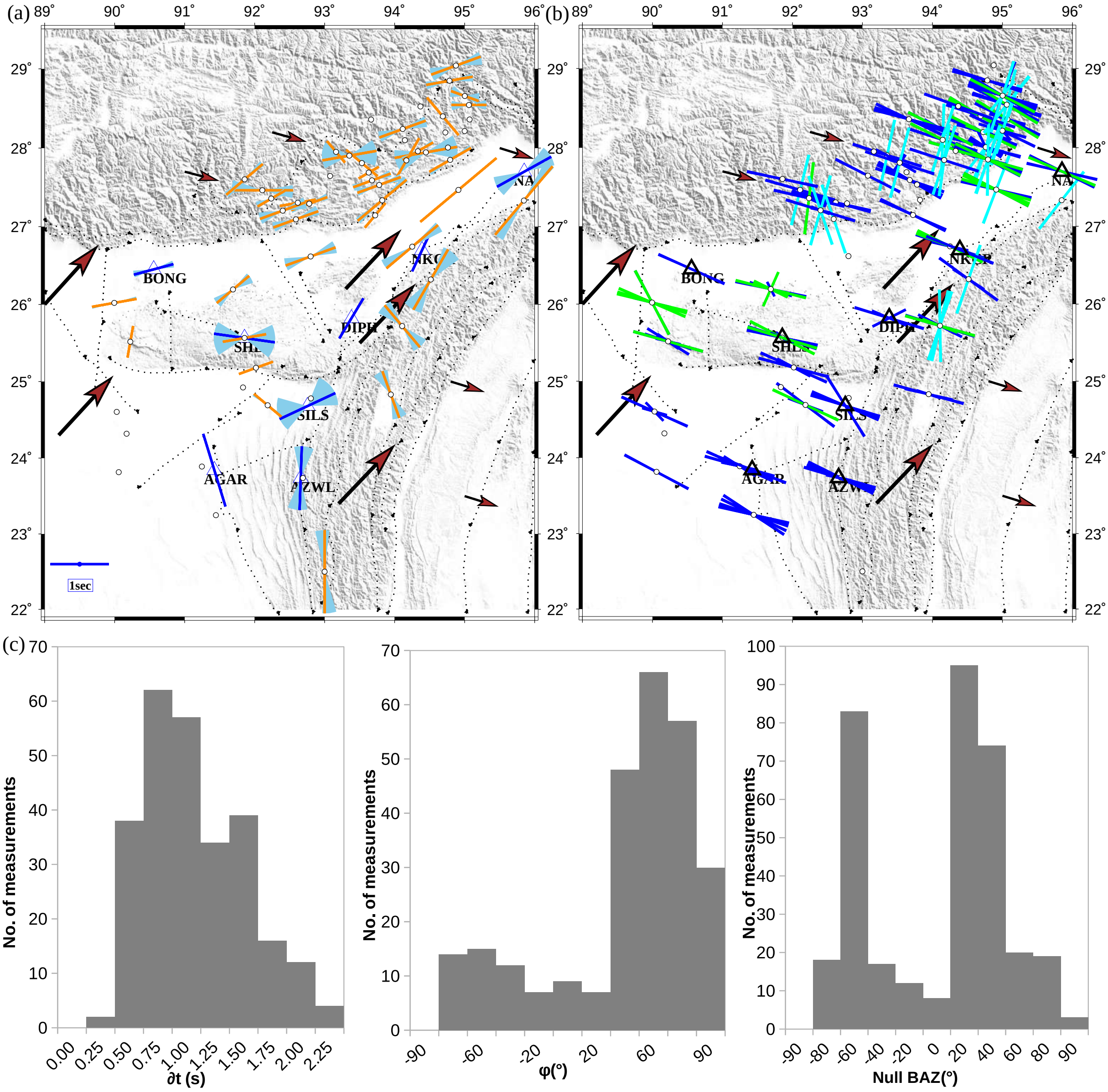

Figure S5. (a) The map shows the apparent station-averaged FPDs(ϕ) plotted at station locations (blue bars are FPD results from IIG stations, orange bars from (Saikia et al., 2018) stations). Bars are scaled with delay times and the oriented in the FPD (ϕ), plotted with associated errors as fans. The small black circles without bars are the stations with only null measurements. (b) The map shows the station-wise Null measurements plotted at station locations (Nulls from SKS, SKKS, and PKS are represented by blue, green, and cyan bars, respectively). Other details are same as in Figure 2. (c) Histogram of the estimated FPD ϕ and delay times δt for the whole dataset. A maximum number of observations indicates the FPD direction lies between 40° and 80° and delay times between 0.7s and 1.25s. The rightmost corner histogram shows the Null results. Null results clearly show the bidirectional distribution of the observed null ϕ direction.

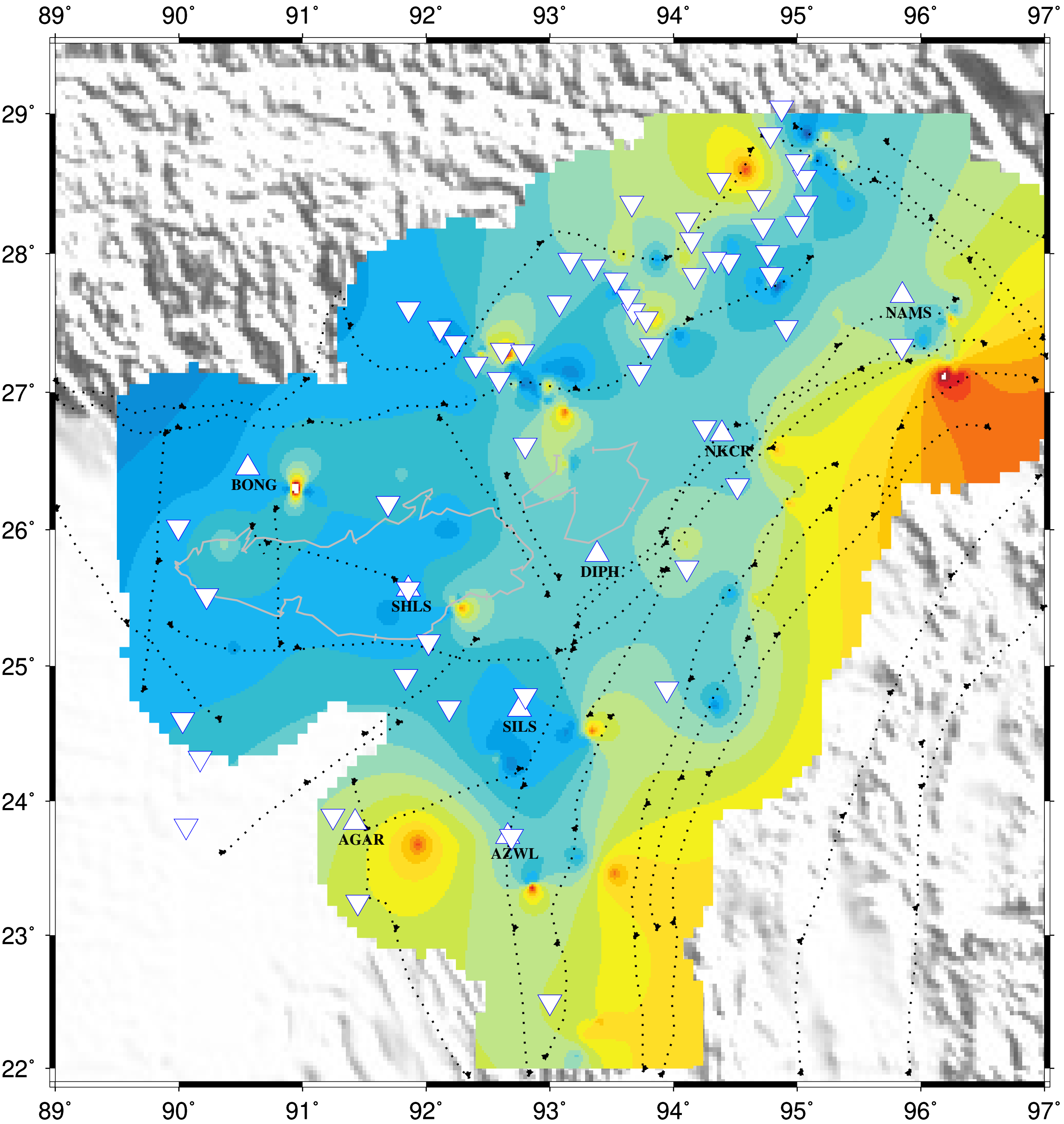

Figure S6. Map of linear interpolation of delay time plotted as a continuous surface plotted on the topographic map of the region with various fault/shear zones. The delay times from individual measurements are plotted above the 200km ray piercing points. Other details are similar to the figure 2.

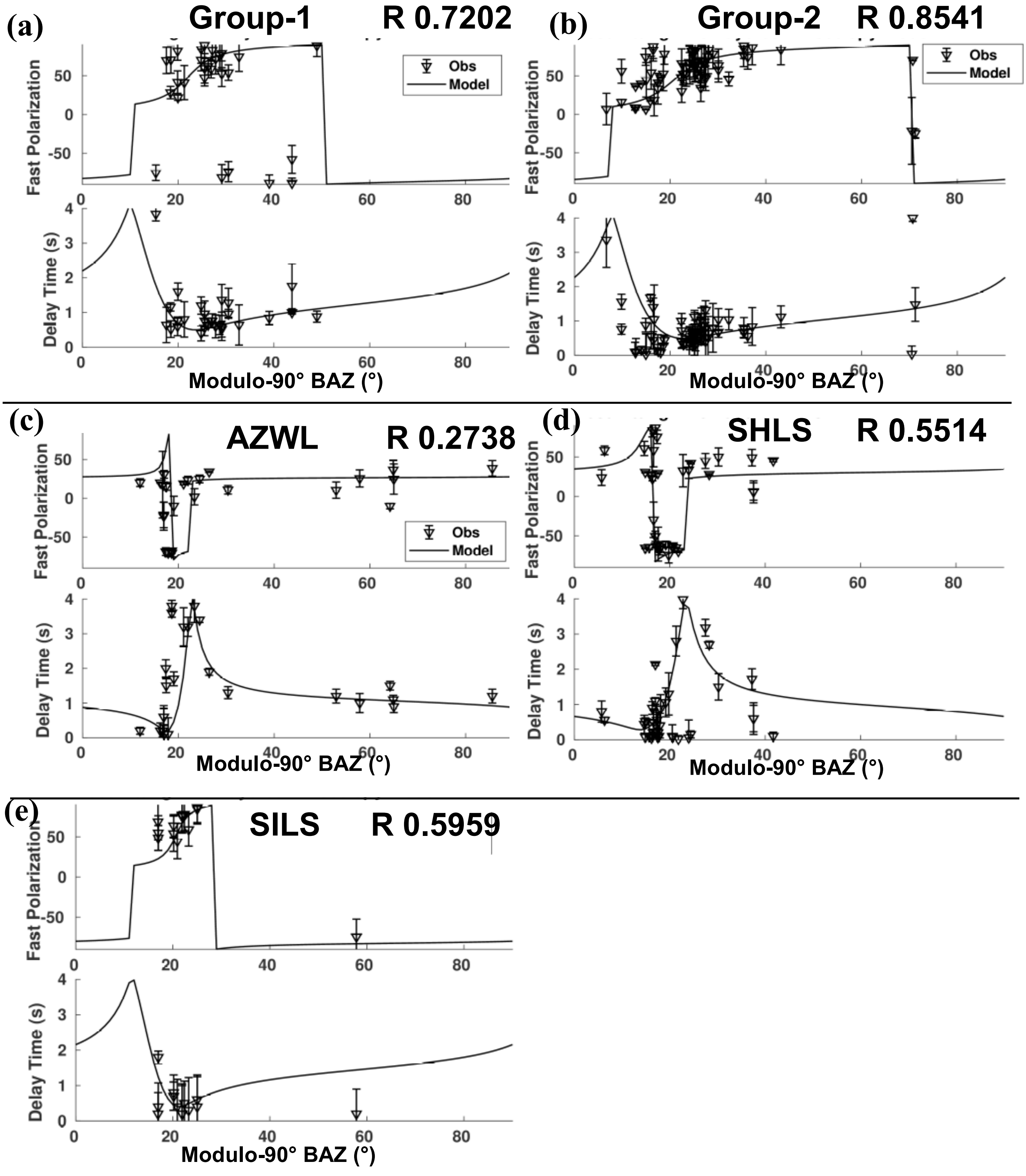

Figure S7. Azimuthal variations of the fast polarization (upper panel) and delay times (lower panel) for stations (a)Group1 (ϕ_U =60, δt_U =0.5; ϕ_L =-66, δt_L =1.2), (b)Group 2 (ϕ_U =60, δt_U =0.7; ϕ_L =-66, δt_L =0.9), (c)AZWL (ϕ_U =35, δt_U =0.4; ϕ_L =15, δt_L =0.7), (d)SHLS (ϕ_U =90, δt_U =0.4; ϕ_L =16, δt_L =1.2), and (e)SILS (ϕ_U =54, δt_U =0.4; ϕ_L =-69, δt_L =1.5). Variation of Fast polarization (FPD) and delay time against the backazimuth (BAZ) are plotted with modulo 90° BAZ values. The curve lines are the best fit model for the apparent splitting measurements